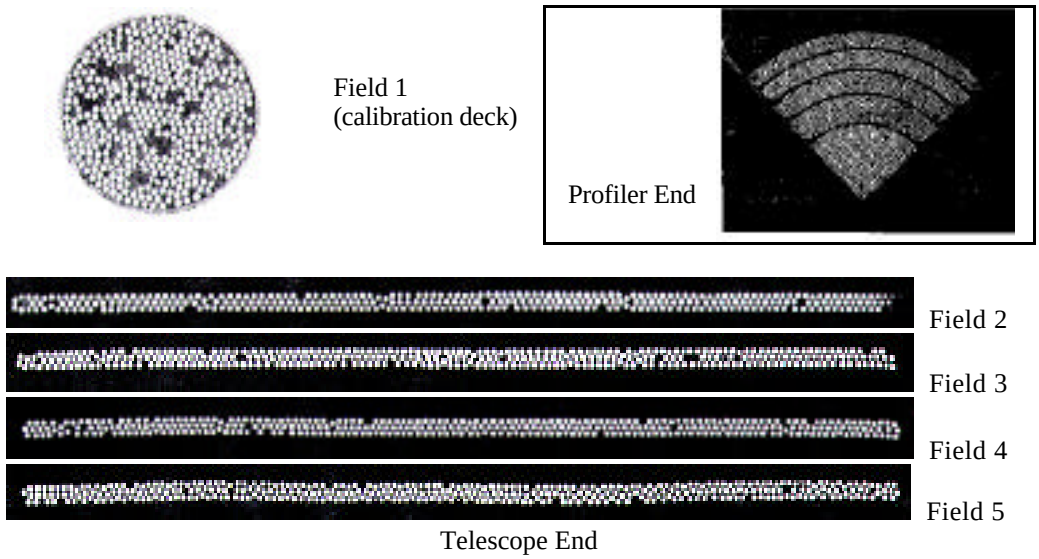


Figure 8. Images of the ends of fiber optic bundle. The number of broken fibers is much less than 10%. Each of the 5 fields at the profiler end are separated by a 50 micron spacer. The calibration field is nearest to the center.

Table 4. Summary of collimating and imaging optics

| Parameter | Value |
|---|---|
| Filter collimator effective focal length | 6.7 cm |
| Etalon collimator effective focal length | 16.7 cm |
| Imaging telescope effective focal length | 59.5 cm |
| Magnification | 3.56 |

Table 5 shows the measured transmittances for these elements. These values are close to expected transmissions.

Table 5. Measured transmittance of optical components

| Element | 836 nm | 786 nm | 633 nm |
|---|---|---|---|
| Input collimator | 0.550 | 0.746 | 0.829 |
| Wideband blocker | 0.937 | 0.954 | 0.902 |
| Imaging optics (Speedring Cassegrain) | 0.917 | 0.940 | 0.980 |
| Product | 0.473 | 0.669 | 0.732 |
| Measured total | 0.50 | 0.48 | 0.70 |

### 3.4. Image Quality

The image quality is quite important for TIDI. Not only the fringe pattern, but also the input optics need to imaged onto the detector because multiple fields are simultaneously imaged onto the detector. If the image quality is not high enough, the image will be smeared across multiple fields resulting in significant cross talk. Figure 9 shows a white light image through the system. The five fields are quite distinct with the dark areas separating them. The vertical columns in each field correspond to the rows of fibers in the input (see Figure 8). The end closest to the apex is the calibration field. The shadowing in the center of the wedge is due to a masking effect of the secondary of the imaging Cassegrain telescope. Figure 10 shows the data from Figure 9 collapsed into a single row, i.e. the signal in a column was averaged.

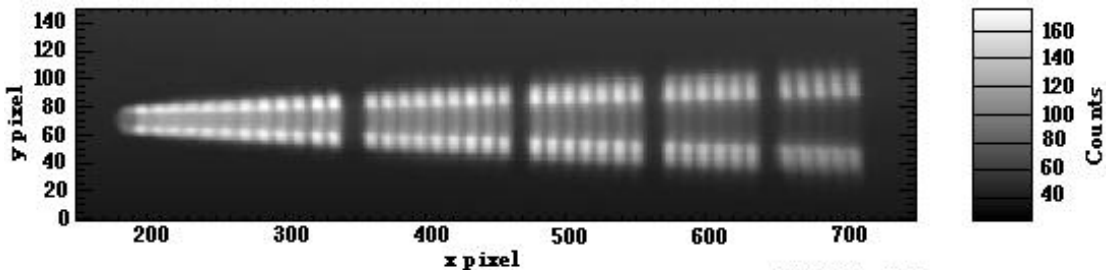


Figure 9. Image of the fiber optic input onto the CCD.

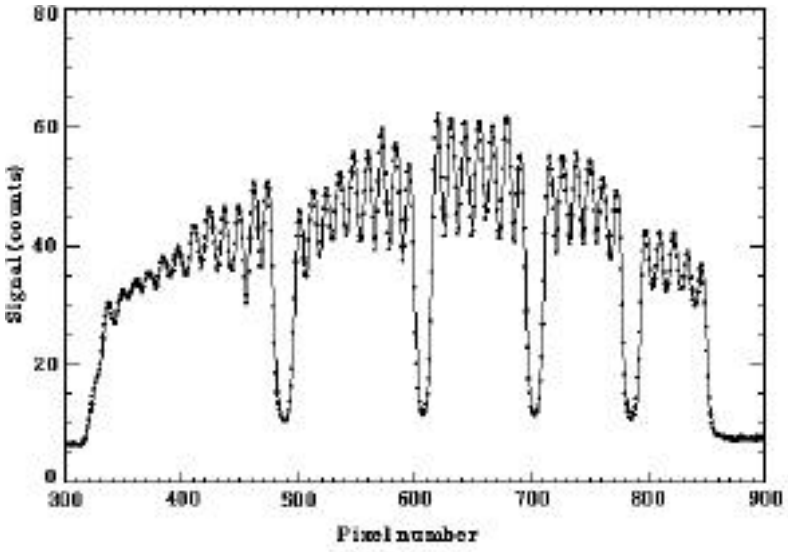


Figure 10. Signal level of data in Figure 9 collapsed into a single row. The x-axis corresponds to the wavelength axis.

### 3.5. CCD Parameters

The TIDI CCD is a SITe model ST-005AB which is a high quantum efficiency, low noise detector. Operationally, the CCD is passively cooled to about -80°C to reduce dark signal and effects of cosmic radiation. The quantum efficiency, charge transfer efficiency (CTE), and dark current of the flight CCD are given in Table 6 and were obtained from the manufacturer (SITe) supplied test data. The parameters were verified by examining an engineering model CCD. The agreement between the measurements and data supplied by SITe was always very good. Figure 11 shows the quantum efficiency measured in the laboratory as a function of wavelength and temperature and compared to the SITe data.

Table 6. Flight CCD parameter summary

| Parameter | Value |
|---|---|
| Manufacturer | SITe |
| Model | ST-005AB |
| Serial number | 8165JCR18-A2 |
| CCD size | 2000 x 800 (1000 x 400 quadrant used) |
| Pixel size | 15 x 15 microns |
| CTE (serial and parallel) | 0.999999 |
| Dark current@20°C | 6.18 pa/cm$^2$, 87 e$^-$ s$^{-1}$ pixel$^{-1}$ |
| QE @400 nm@T=-80°C | 70.52% |
| QE @500 nm@T=-80°C | 74.80% |
| QE @600 nm @T=-80°C | 67.64% |
| QE @700 nm @T=-80°C | 76.36% |
| QE @800 nm @T=-80°C | 62.80% |
| QE @900 nm @T=-80°C | 36.00% |
| Read noise | 7 e$^-$ |
| Illumination | backside |
| MPP | yes |
| AR coating | standard visible |
| Full well capacity (parallel) | 64 ke$^-$ |
| Full well capacity (serial) | 800 ke$^-$ |
| Operating temperature | -80°C (passively cooled) |

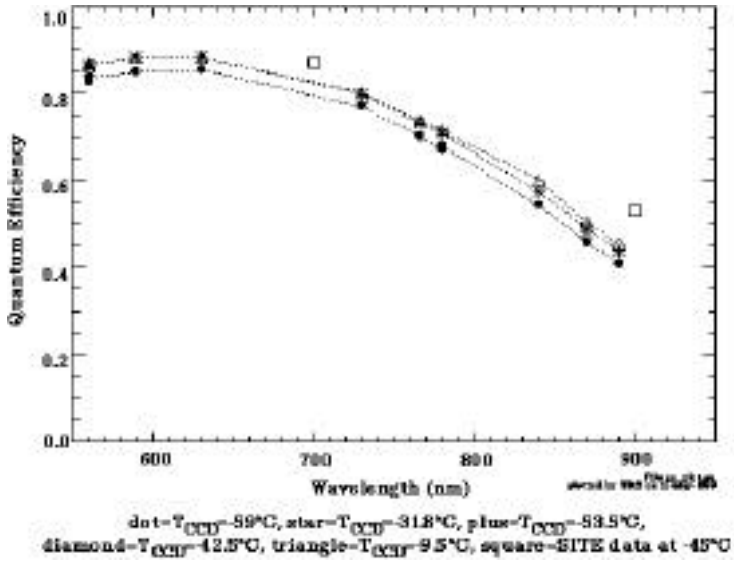


Figure 11. Measured quantum efficiency for an engineering CCD.

The TIDI CCD controller supports four gain settings for converting image data from the CCD to digital values. Table 7 shows the CCD Controller A/D converter rates, gain, and approximate bias levels for each of the gain settings. The A/D is a 12-bit system which has a range of 0-4095 counts. The four gain settings were chosen to allow a choice between a high sensitivity, relatively small dynamic range and a low sensitivity, large dynamic range. The gain of 160 $e^-$/count provides a dynamic range ($6.55 \times 10^5$ $e^-$) that nearly matches that of serial register output ($8 \times 10^5$ $e^-$). The gains of 5 and 10 $e^-$/count are near the read noise value of approximately 7 $e^-$/count and provide a high sensitivity with a reasonably large dynamic range. The gain of 40 $e^-$/count provides an intermediate value.

Table 7. TIDI CCD gain settings

| Gain setting | Readout Rate (KHz) | System Gain ($e^-$/count) | Approximate bias level (counts) | Readout time (s) |
|---|---|---|---|---|
| 1 | 64 | 160 | 10.5 | 0.096 |
| 2 | 32 | 40 | 28.5 | 0.100 |
| 3 | 8 | 10 | 120 | 0.111 |
| 4 | 4 | 5 | 253 | 0.126 |

The readout capability of the CCD is very flexible. It is possible to collect an image of any 600x50 region of any part of the working quadrant of the CCD. With this capability it is possible to examine the details of the image on the CCD. Complete images are infrequently collected for calibrations or for diagnosing problems. The readout of the CCD is relatively slow and the telemetry rate is sufficient for only 150 pixels per second. Normally, the signal is integrated on the chip. The image of the etalon forms a wedge on the CCD which is about 667 pixels in the wavelength (x) direction and a maximum of 66 pixels in the perpendicular (y) direction. The location of this wedge is determined during calibration and only this region is read out. The desired image lies in a wedge, but because of the design of the controller it is necessary to read out a rectangular region. All the pixels in the y direction are summed on the chip which reduces read noise and decreases the readout time. The binning in the x direction is under complete control of the user and it is possible to combine different numbers of pixels in the x direction. The binning can be arranged so that each readout contains nearly an equal wavelength interval. The TIDI binning pattern will divide each of the five fields of the CCD into 30 spectral channels. The innermost field (closest to the center of the fringe) will have about 166 pixels to be divided, while the outer one has only 60.

### 3.5. Filters

The TIDI filters isolate spectral lines for examination by the interferometer. All TIDI filters were constructed by Barr Associates. There are two filter wheels, each containing 8 filters. Since the light must pass through each wheel, one position of each contains a Schott glass OG 515 filter that has been AR coated. This transmits all wavelengths of interest to TIDI while reducing unwanted light from short wavelengths. Additional wideband blocking is provided by a filter that isolates the spectral region 550-900 nm. This filter is mounted in the collimating optics and not on the filter wheel. Figure

12 shows the transmission curve for this filter and Figure 13 shows a narrowband (0.3 nm) filter for use in the $O_2$ (0-0) band. The 14 filters that are designated for science investigations are summarized in Table 8. Many filters transmit calibration lines from argon, krypton, or neon which are part of the calibration system. The filters are tilted by 1 degree relative to the optical axis to direct the reflected light out of the optical path. The filters are constructed of metal oxide material which are very durable and have a low thermal drift coefficient. The thermal drifts are about a factor of 10 lower than the filters used by DE-FPI and HRDI/UARS. This reduces the requirement for instrument control significantly. The requirement for the TIDI instrument is $\pm 5^{o}$C about a nominal operating temperature of $20^{o}$C.

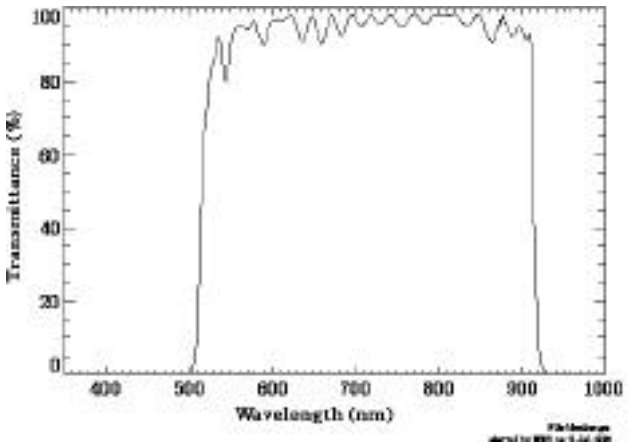


Figure 12. Transmission curve for wideband blocker

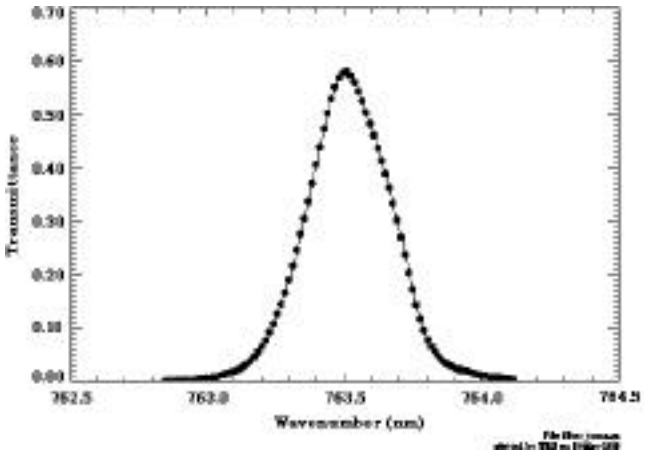


Figure 13. Measured transmission curve for a narrow band $O_2$ (0-0) filter.

Table 8. TIDI filter summary

| Filter wheel and position | Filter center wavelength (in air) (nm) | Emissions | Bandwidth (full width half maximum) (nm) | Peak transmittance |
|---|---|---|---|---|
| 1-1 | 867.13 | $O_2(^1\Sigma)$ (0-1) P11 pair and argon (866.79 nm) | 0.35 | 0.56 |
| 1-2 | 763.62 | $O_2(^1\Sigma)$ (0-0) P9 pair and argon (763.51 nm) | 0.32 | 0.62 |
| 1-3 | 557.89 | OI ($^1$S) | 0.55 | 0.85 |
| 1-4 | OG 515 | short wavelength blocker | | |
| 1-5 | 630.23 | OI ($^1$D) and neon (630.48 nm) | 0.62 | 0.77 |
| 1-6 | 765.20 | $O_2(^1\Sigma)$ (0-0) P15 pair | 0.30 | 0.70 |
| 1-7 | 866.14 | $O_2(^1\Sigma)$ (0-1) P7 pair and argon (866.79 nm) | 0.36 | 0.57 |
| 1-8 | 892.01 | OH Meinel (7-3) P1(3) pair and neon (891.95 nm) | 0.55 | 0.76 |
| 2-1 | OG 515 | short wavelength blocker | | |
| 2-2 | 732.04 | OII ($^2$P) pair | 0.58 | 0.58 |
| 2-3 | 844.70 | OI triplet | 0.61 | 0.67 |
| 2-4 | 557.28 | OI ($^1$S) cal filter krypton (557.03 nm) | 0.65 | 0.53 |
| 2-5 | 589.37 | NaD doublet and neon (590.25 nm) | 1.01 | 0.61 |
| 2-6 | 779.60 | OH Meinel (9-4) P1(2) pair | 0.73 | 0.71 |
| 2-7 | 763.92 | $O_2(^1\Sigma)$ (0-0) P branch and argon (763.51 nm) | 3.95 | 0.79 |
| 2-8 | 760.51 | $O_2(^1\Sigma)$ (0-0) R branch and krypton (760.15 nm) | 1.92 | 0.81 |

### 3.7. CLIO Cone

The CLIO cone converts the fringe pattern to a relatively narrow wedge on the CCD. It has an apex angle of 45 degrees and extends 180 degrees. Only 90 degrees are used optically, with the material in the rest of the cone providing radiation shielding for the CCD. The cone is constructed from aluminum and overcoated with nickel. This was diamond turned to a finish with an rms roughness of about 3 nm. No polishing of the surface was performed. The surface was overcoated with Denton FSS-99 coating which is a silver and dielectic coating and gives the cone a reflectivity of greater than 95% throughout the region of interest.

### 3.8. Etalon

The etalon is the spectrally resolving element of the interferometer. Optically, the TIDI etalon was optimized for mesospheric wind observations using the $O_2$ Atmospheric (0,0) band around 762 nm. The optimization procedure specified a gap thickness of 2.2 cm and the reflectivity of about 80%. The actual reflectivity curve is shown in Figure 14. The etalon requires a 7.5 cm clear aperture to accept the light from all four telescopes and the calibration field. The etalon is constructed out of fused silica and the posts are made of zerodur. This is the same as the DE-FPI etalon and the fixed etalon of HRDI/UARS. Similar to DE-FPI, but unlike HRDI/UARS which used optical contacts, the posts are cemented to the plates with about a 1-micron thick layer of Norland 61 UV setting epoxy. The mount is similar to the design used by DE-FPI.[6,7] The etalon characteristics are summarized in Table 9.

Table 9. Etalon parameter summary

| Parameter | Value |
|---|---|
| Plate material | fused silica (Supersil-B) |
| Post material | zerodur |
| Plate diameter | 10.5 cm |
| Coated area diameter | 8.6 cm |
| Back surface wedge angle | 0.9 degree |
| Plate thickness | 2.54 cm |
| Post length | 2.2 cm |
| Post to plate contact | ~1 micron thick epoxy layer (Norland 61) (no optical contact) |

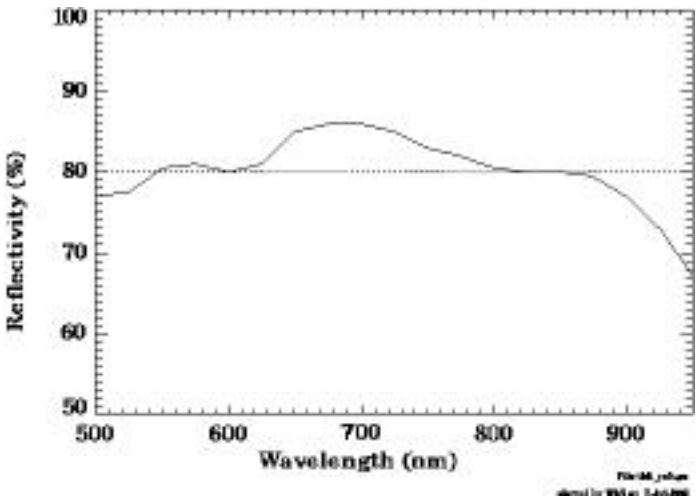


Figure 14. Measured reflectivity of the TIDI etalon plates.

## 4. SYSTEM CHARACTERISTICS

### 4.1. Spectral Resolution

An image of the interference pattern of a frequency stabilized helium neon laser is shown in Figure 15. The x scale is non-linear in wavelength so the fringes at the left side of the image (smaller pixel numbers) appear broader. This test configuration filled more of the CCD than will be used operationally, and only the first seven orders (counting from the left)

are used operationally. Figure 16 shows the data collapsed into a single line, remapped so the x axis is linear with wavelength. The derived finesses are slightly lower than hoped for, but still acceptable. Other tests (not shown here) demonstrate the finesse increases at longer wavelengths, consistent with plate distortions being a major component of the overall finesse.

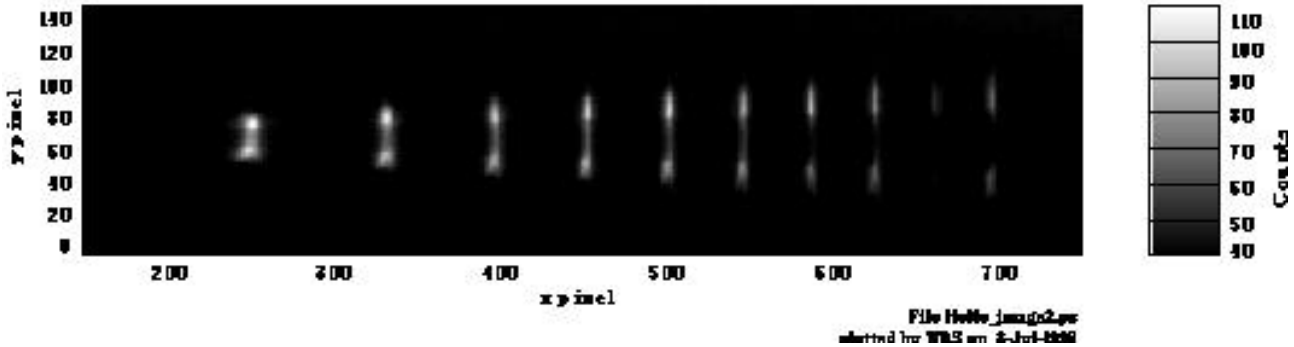


Figure 15. Image of a He-Ne laser input.

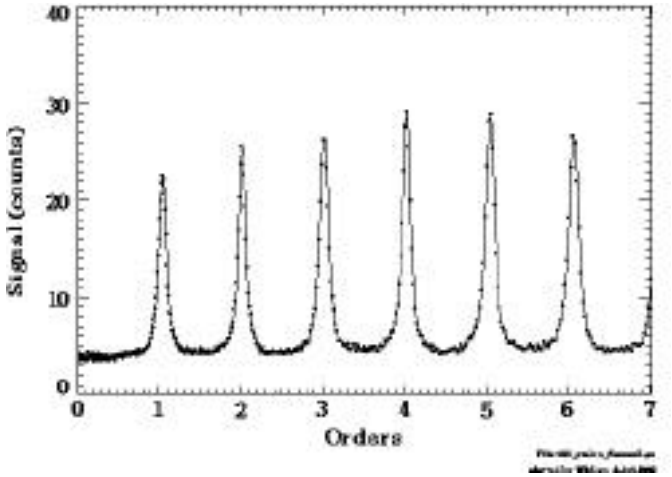


Figure 16. He-Ne laser light mapped so the x axis is linear in wavelength. The data used filled more of the CCD than actually used in normal operations so only the first 7 orders provide meaningful finesse values.

### 4.2. Estimated Sensitivity

The TIDI calibrations are not complete at the time of this writing so the final sensitivity numbers for the instrument are not available. Using the values presented in the previous sections it is possible to estimate the throughput and sensitivity to Doppler shifts. Here a simplified form of the TIDI instrument function is presented to illustrate how the various parameters discussed in the previous sections contribute to the overall instrument performance. The signal, C, on any spectral channel, j, can be expressed as the convolution of the Fabry-Perot transmission function and the illumination source multiplied by appropriate throughput factors:

$$C(j) = S\left(\frac{1-R}{1+R}\right)\Delta t\left(1+2\sum_{n=1}^{\infty} R^n \exp\left(-4\pi^2 n^2 t^2 \alpha_D^2 - \frac{\pi^2 n^2}{4N_D^2 \ln 2}\right)\sin c\left(\frac{\pi n}{N_A}\right)\sin c\left(\frac{\pi n}{N_{FOV}}\right)\cos\left(2\pi n\left(\frac{j}{N_A}\right) - \varphi\right)\right) \quad (1)$$

where $\Delta t$ is the integration time, $\varphi$ is a phase term which locates the position of the fringe peak on the detector (the wind information is in this term) and the other terms are defined in Tables 10 and 11. The sensitivity, S, is given by

$$S(\lambda) = \frac{A\Omega 10^6}{4\pi n_{chan}} T_{tele}(\lambda) T_{fiber}(\lambda) T_{coll}(\lambda) T_{wb}(\lambda) T_{fil}(\lambda) T_{im}(\lambda) R_{cone}(\lambda) Q(\lambda) T_{margin} \quad (2)$$

where k is the gain (Table 7). This formulation assumes that the area-solid angle product for all channels is the same, which is only an approximation since the number of CCD pixels per channel must be an integer. The 1/e width of a spectral line is given by

$$\alpha_D = 4.30\text{x}10^{-7}\,\nu_o\left(\frac{T}{M}\right)^{1/2} \tag{3}$$

where $\nu_o$ is the central wavenumber, T is the emitter temperature and M is the atomic mass.

The aperture finesse is the number of channels used to cover a free spectral range of the etalon. The aperture finesse varies slightly with channel number because of the discreteness of the CCD pixels, but to a good approximation can be expressed as a constant across the field. The optical system was designed so that 1.2 orders covered 30 spectral channels at 900 nm. The aperture finesse at any other wavelength is

$$N_A(\nu) = N_A(\nu_o)\frac{\nu_o}{\nu} = N_A(\lambda_o)\frac{\lambda}{\lambda_o} \tag{4}$$

which gives nearly 2 orders at 557 nm. A minimum of 1.2 orders was chosen to be sure the line was well defined even if it was near the edge of the field. Since the TIDI etalon is a fixed gap etalon, there is no way to adjust the line position.

The defect finesse is caused by distortion of the plates. This is particularly important for a spaceflight etalon since it must be held securely during launch to prevent breaking. This requires a firm mounting which can significantly distort the plates. The defect finesse has not been evaluated for TIDI, but it is expected that the overall instrument finesse will be about 10, and the modeling presented here assumes a corresponding defect finesse. The defect finesse (whatever its exact form) has a linear scaling factor with wavelength

$$N_D(\nu) = N_D(\nu_o)\frac{\nu_o}{\nu} = N_D(\lambda_o)\frac{\lambda}{\lambda_o}\,. \tag{5}$$

The field of view finesse is the spectral broadening caused by the differing spacecraft velocity motion component from one end of the field of view to the other. This causes a varying Doppler shift across the field. The light is spatially scrambled by the fiber bundle and this effect acts as a broadening of the fringe. In order to calculate it properly, field of view maps such as shown in Figure 5 must be numerically integrated. To provide an estimate of the effect, a rectangular field of view is assumed with uniform contributions from all locations in the field. In that case a field of view finesse can be defined by

$$N_{FOV} = \frac{c}{2t\nu_o v_{sat}\cos\theta_{dep}\sin\theta_{az}\Delta\theta_{az}}\,. \tag{6}$$

Tables 10 and 11 show the values that allow the throughput and finesse to be calculated for representative wavelengths through the TIDI operating range. Also shown in Table 11 is the Doppler shift error for a 10-kR line viewed for 1 s. This is not intended to be representative of the TIDI errors, but to show for a given input how the errors will vary due to changing wavelengths and different emissions.

## 5. CONCLUSION

This paper has briefly described the TIDI optical design and the performance of some of the optical components. The TIDI design is very efficient, using the light from all 4 telescopes simultaneously, using high quality optical components and a high sensitivity CCD detector. The analysis of the characteristics of the elements indicate that TIDI will able to fully meet the scientific goals. Further information on the TIMED program and TIDI project can be obtained from the web sites http://www.sprl.umich.edu/TIDI and http://www.timed.jhuapl.edu.

## 6. ACKNOWLEDGMENTS

This work was supported by NASA contract NAG5-5049 to the University of Michigan.

Table 10. TIDI estimated transmittance and throughput parameters

| Parameter | 550 nm | 630 nm | 760 nm | 860 nm | 890 nm |
|---|---|---|---|---|---|
| Telescope diameter (cm) | 7.5 | 7.5 | 7.5 | 7.5 | 7.5 |
| Telescope effective area ($cm^2$) (A) | 44.2 | 44.2 | 44.2 | 44.2 | 44.2 |
| Field of view (degrees) | 2.5 x 0.05 | 2.5 x 0.05 | 2.5 x 0.05 | 2.5 x 0.05 | 2.5 x 0.05 |
| field of view (sr) ($\Omega$) | $3.81 \times 10^{-5}$ | $3.81 \times 10^{-5}$ | $3.81 \times 10^{-5}$ | $3.81 \times 10^{-5}$ | $3.81 \times 10^{-5}$ |
| Telescope area - field of view product ($cm^2$ sr) | $1.68 \times 10^{-3}$ | $1.68 \times 10^{-3}$ | $1.68 \times 10^{-3}$ | $1.68 \times 10^{-3}$ | $1.68 \times 10^{-3}$ |
| Telescope transmittance ($T_{tele}$) | 0.49 | 0.78 | 0.93 | 0.93 | 0.93 |
| Fiber optic transmittance ($T_{fiber}$) | 0.49 | 0.49 | 0.45 | 0.42 | 0.41 |
| Collimator transmittance ($T_{coll}$) | 0.87 | 0.83 | 0.76 | 0.53 | 0.51 |
| Wide band blocker transmittance ($T_{wb}$) | 0.90 | 0.90 | 0.95 | 0.92 | 0.91 |
| Filter peak transmittance ($T_{fil}$) | 0.85 | 0.77 | 0.62 | 0.56 | 0.76 |
| Imaging optics transmittance ($T_{im}$) | 0.98 | 0.98 | 0.95 | 0.91 | 0.90 |
| CLIO cone reflectivity ($R_{cone}$) | 0.95 | 0.95 | 0.95 | 0.95 | 0.95 |
| Factor for other transmission losses ($T_{margin}$) | 0.75 | 0.75 | 0.75 | 0.75 | 0.75 |
| Optics transmittance ($T_{opt}$) | 0.11 | 0.15 | 0.13 | 0.07 | 0.09 |
| Detector quantum efficiency (Q) | 0.71 | 0.70 | 0.68 | 0.47 | 0.39 |
| number of detector channels per field, ($n_{chan}$) | 30 | 30 | 30 | 30 | 30 |
| Sensitivity ($e^- s^{-1}$ channel$^{-1}$ $R^{-1}$) (S) | 0.47 | 0.64 | 0.51 | 0.20 | 0.23 |

Table 11. Estimated spectral properties of the TIDI interferometer system

| Parameter | 550 nm | 630 nm | 760 nm | 860 nm | 890 nm |
|---|---|---|---|---|---|
| Etalon gap spacing (t) | 2.2 cm | 2.2 cm | 2.2 cm | 2.2 cm | 2.2 cm |
| Reflectivity, (R) | 0.805 | 0.818 | 0.826 | 0.798 | 0.780 |
| Reflectivity finesse $N_R$ | 14.5 | 15.6 | 16.4 | 13.9 | 12.6 |
| Number of orders on detector for each field | 2.0 | 1.7 | 1.4 | 1.3 | 1.2 |
| Aperture finesse (spectral channels/order) ($N_A$) | 15.3 | 17.5 | 21.1 | 23.9 | 24.7 |
| Defect finesse ($N_D$) | 18.3 | 21.0 | 25.3 | 28.7 | 29.7 |
| Satellite speed ($v_{sat}$) | 7500 $ms^{-1}$ | 7500 $ms^{-1}$ | 7500 $ms^{-1}$ | 7500 $ms^{-1}$ | 7500 $ms^{-1}$ |
| Depression angle from horizontal ($\theta_{dep}$) | $21^o$ | $21^o$ | $21^o$ | $21^o$ | $21^o$ |
| Azimuth angle from velocity vector($\theta_{az}$) | $45^o$ | $45^o$ | $45^o$ | $45^o$ | $45^o$ |
| Horizontal field width $\Delta\theta_{az}$ | $2.5^o$ | $2.5^o$ | $2.5^o$ | $2.5^o$ | $2.5^o$ |
| Field of view finesse ($N_{FOV}$) | 17.3 | 19.9 | 24.0 | 27.1 | 28.1 |
| Total finesse | 8.0 | 8.9 | 9.9 | 9.3 | 8.9 |
| Etalon peak transmittance | 0.66 | 0.67 | 0.72 | 0.80 | 0.83 |
| Emitter | O | O | $O_2$ | $O_2$ | OH |
| Atomic mass, (M) | 16 | 16 | 32 | 32 | 18 |
| Representative temperature (T) | 200 K | 1000 K | 180 K | 180 K | 180 K |
| 1/e linewidth ($\alpha_D$) | 0.028 $cm^{-1}$ | 0.054 $cm^{-1}$ | 0.013 $cm^{-1}$ | 0.012 $cm^{-1}$ | 0.015 $cm^{-1}$ |
| Error for 10kR line brightness | 4.7 $ms^{-1}$ | 7.9 $ms^{-1}$ | 4.9 $ms^{-1}$ | 7.8 $ms^{-1}$ | 8.7 $ms^{-1}$ |

## 7. REFERENCES


1. J.-H. Yee, G. E. Cameron, and D. Y. Kusnierkiewicz, "An Overview of TIMED," *SPIE 3756* (this issue), 1999.
2. P. B. Hays, T. L. Killeen, and B. C. Kennedy, "The Fabry-Perot Interferometer on Dynamics Explorer," *Space Sci. Instrumentation 5*, pp. 395-416, 1981.
3. P. B. Hays, V.J. Abreu, M.E. Dobbs, D.A. Gell, H.J. Grassl, and W.R. Skinner, "The High Resolution Doppler Imager on the Upper Atmosphere Research Satellite," *J. Geophys. Res. 98*, pp. 10,713-10,723, 1993.
4. H. J. Grassl, W. R. Skinner, P. B. Hays, M. D. Burrage, D. A. Gell, A. R. Marshall, D. A. Ortland, and V. J. Abreu, "Atmospheric wind measurements with the High Resolution Doppler Imager (HRDI)," *J. Spacecraft & Rockets 32*, No. 1, pp. 169-176, Jan.-Feb. 1995.
5. P. B. Hays, "Circle to line interferometer optical system," *Appl. Opt. 29*, pp. 1482-1489, 1990.
6. T. K. Killeen, P. B. Hays, B. C. Kennedy, and D. Rees, "Stable and rugged etalon for the Dynamics Explorer Fabry-Perot interferometer. 2: Performance," *Appl. Opt. 21*, pp. 3903-3912, 1982.
7. D. Rees, T. J. Fuller-Rowell, A. Lyons, T. L. Killeen, and P. B. Hays, "Stable and rugged etalon for the Dynamics Explorer Fabry-Perot interferometer. 1: Design and construction," *Appl. Opt. 21*, pp. 3896-3902, 1982.